

# Terahertz-Induced Tunnel Ionization Drives Coherent Raman-Active Phonon in Bismuth

Bing Cheng,<sup>1,\*</sup> Patrick L. Kramer,<sup>2</sup> Mariano Trigo,<sup>1,3</sup> Mengkun Liu,<sup>4</sup> David A. Reis,<sup>1,3</sup> Zhi-Xun Shen,<sup>1,5,6</sup> Jonathan A. Sobota,<sup>1,†</sup> and Matthias. C. Hoffmann<sup>2,‡</sup>

<sup>1</sup>*Stanford Institute for Materials and Energy Sciences,*

*SLAC National Accelerator Laboratory, Menlo Park, CA 94025, USA*

<sup>2</sup>*Laser Science and Technology, SLAC National Accelerator Laboratory, Menlo Park, CA 94025, USA*

<sup>3</sup>*PULSE Institute, SLAC National Accelerator Laboratory, Menlo Park, CA, 94025, USA*

<sup>4</sup>*Department of Physics and Astronomy, Stony Brook University; Stony Brook, New York 11794, USA*

<sup>5</sup>*Geballe Laboratory for Advanced Materials, Stanford University, Stanford, CA 94305, USA*

<sup>6</sup>*Departments of Physics and Applied Physics Stanford University, Stanford, California 94305, USA*

(Dated: September 18, 2024)

Driving coherent lattice motion with THz pulses has emerged as a novel pathway for achieving dynamic stabilization of exotic phases that are inaccessible in equilibrium quantum materials. In this work, we present a previously unexplored mechanism for THz excitation of Raman-active phonons in semimetals. We show that intense THz pulses centered at 1 THz can excite the Raman-active  $A_{1g}$  phonon mode at 2.9 THz in a bismuth film. We rule out the possibilities of the phonon being excited through conventional anharmonic coupling to other modes or via a THz sum frequency process. Instead, we demonstrate that the THz-driven tunnel ionization provides a plausible means of creating a displacive driving force to initiate the phonon oscillations. Our work highlights a new mechanism for exciting coherent phonons, offering potential for dynamic control over the electronic and structural properties of semimetals and narrow-band semiconductors on ultrafast timescales.

The use of ultrafast laser pulses to excite and manipulate coherent phonons presents a promising approach for dynamically controlling the electronic and structural properties of quantum materials [1–4]. As a result, the exploration of phonon driving mechanisms across different materials has become an important research subject. For the excitation of Raman-active phonons via femtosecond laser pulses at visible or near-infrared wavelengths, two primary excitation mechanisms, impulsive stimulated Raman scattering (ISRS)[5, 6] and displacive excitation of coherent phonons (DECP)[7, 8], have been extensively discussed in the literature. The excitation of coherent phonons via ISRS is described by the equation in the single impulse limit:  $\frac{d^2 Q}{dt^2} + \Omega^2 Q = \frac{1}{2} \left( \frac{\partial \chi}{\partial Q} \right) |E_0(\mathbf{r}, t)|^2$ . Here  $Q$  is the amplitude of the Raman-active phonon mode,  $\Omega$  is the phonon frequency,  $E_0$  is the driving electric field of the laser pulse and  $\chi$  is the electronic susceptibility. This equation indicates that the lattice motion of the Raman phonon is controlled by the Fourier components of the driving force at frequency  $\Omega$ . Efficient excitation is only possible when the laser pulse duration is short compared with  $\Omega^{-1}$  and there is a sufficiently large coupling of the phonon coordinate  $Q$  with the susceptibility  $\chi$ . On the other hand, in the DECP picture, the driving force of coherent phonon comes from the laser-induced sudden change of the carrier density or the effective electronic temperature[7]. If this laser-induced sudden change is fast enough, the ions will be driven to a new quasi-equilibrium position in a time scale shorter than  $\Omega^{-1}$ . Such an ultrafast change of ion position generates a restoring force for the coherent atomic motion of the Raman phonon.

Despite the well-established ISRS and DECP mechanisms, the recent observations of THz driving Raman-active phonons in solids are challenging these simple pictures [9–15]. The oscillation cycle of THz pulses generated by the tilted pulse front method is approximately 1 ps [16]. Based on the assumptions of ISRS and DECP, it is somewhat counterintuitive to see such “slow” THz pulses drive Raman-active phonons above 1 THz. However, in some metallic materials like doped  $\text{Bi}_2\text{Se}_3$ , intense THz pulses have been found to drive Raman-active phonon modes at 2.05 THz and 4.05 THz [12, 14]. Competing mechanisms have been proposed to understand these unusual observations. The first proposal involves an anharmonic phonon coupling model. In this model, the intense THz pulses first excite an infrared-active zone center phonon mode [12, 14]. The anharmonic interactions between the phonons allow the THz-driven oscillations of the infrared-active mode to serve as an effective driving force to launch Raman-active phonon modes. Another mechanism under consideration is THz sum frequency generation. In this process, the excitation of Raman-active modes occurs directly through the absorption of two THz photons that does not require the intermediary action of other phonons [11, 13]. Both this model and the anharmonic phonon coupling model have been effective in elucidating various nonlinear phononic and photonic phenomena observed in dielectrics [13, 17].

In this work, we investigate a novel but previously-unexplored mechanism for excitation of Raman-active phonons in semimetallic bismuth thin films through THz pulses. Bismuth is a prototypic material that has been extensively investigated by various ultrafast and nonlin-

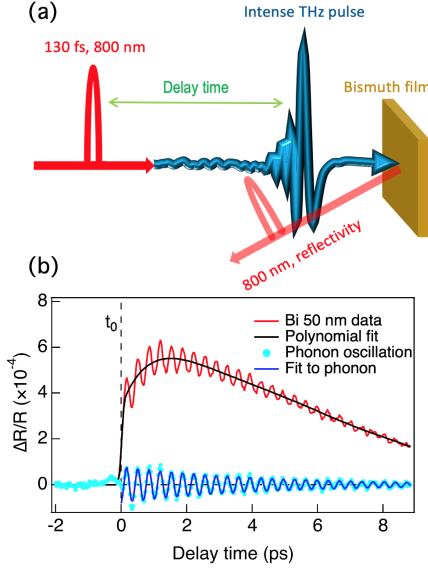


FIG. 1. (a) Schematic of THz pump optical probe spectroscopy. (b) THz-induced reflectivity change  $\Delta R/R$  of a 50 nm thick bismuth film as a function of pump-probe delay time at 400 kV/cm. We use a cosine function to fit the phonon oscillation isolated by a polynomial fit. The initial phase of the phonon oscillation is found to be  $(0.035 \pm 0.009)\pi$ .

ear spectroscopies [2, 3, 18–23]. Previous optical pump-probe experiments on bismuth identified two Raman-active phonons: an  $E_g$  mode at 2.1 THz and an  $A_{1g}$  mode at 2.9 THz [18–21]. Using THz-pump optical-probe spectroscopy, we observed long-lived coherent oscillations of the  $A_{1g}$  mode at 2.9 THz in reflectivity at 800 nm. Our analysis suggests that the excitation of the  $A_{1g}$  mode is likely due to THz-induced tunnel ionization, which rapidly increases carrier density and consequently triggers the phonon.

Our 50 nm thick c-axis Bi film was grown on a  $1 \times 1$  cm<sup>2</sup> sapphire substrate. The sample is similar to the ones used in Ref. [21]. We used single-cycle THz pulses up to 500 kV/cm generated from optical rectification in LiNbO<sub>3</sub> to excite Bi film. The pump-induced reflectivity change was probed by a 130 fs, 800 nm pulse as a function of time delay with respect to the THz pump pulse. The schematic of our THz pump optical probe setup is shown in Figs. 1(a). More details are provided in Supplementary Material (SM). All measurements in this work were performed at room temperature. Figure 1(b) shows the reflectivity change,  $\Delta R/R$ , as a function of delay time at a THz field strength of 400 kV/cm. The polarization of the probe pulse was perpendicular to that of the THz pulse. Following a fast initial rise, clear coherent phonon oscillations with a period of 340 fs are observed against a slowly decaying electronic background. These oscillations correspond to a mode frequency of 2.9 THz (Figs. 2(b)), which aligns with the well-known  $A_{1g}$

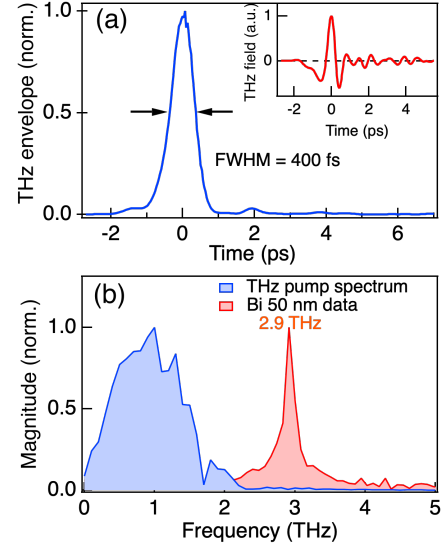


FIG. 2. (a) The THz pulse width is defined by the full width at half maximum (FWHM) of the square of the Hilbert transform of the THz field. The inset shows THz field measured by electro-optic sampling. (b) Spectral magnitude of phonon oscillations (red) and THz pulse (blue) obtained by Fourier transform.

Raman-active mode in bismuth. At the frequency corresponding to the  $A_{1g}$  phonon, the THz field strength is about 1% of its peak value.

Figure 2(a) displays the THz intensity, defined as the square of the field envelope. This envelope was derived from an electro-optical measurement of the THz field at the sample location (inset) using Hilbert transformation. Notably, the full width at half maximum (FWHM) of the THz intensity is 400 fs, which exceeds the oscillation period of the bismuth  $A_{1g}$  phonon (340 fs). As a result, THz pulses cannot drive rapid enough changes in carrier density or electronic temperature to launch the Raman-active phonon as laser pulses at visible or near-infrared wavelengths do. We need to explore models beyond conventional mechanisms to understand how this  $A_{1g}$  phonon mode is driven by THz pulses.

In order to elucidate the excitation mechanism, we carried out a THz field strength dependent study. Figure 3(a) shows representative time traces of reflectivity change  $\Delta R/R$  at two different pump field strengths. At a field strength of 290 kV/cm, a sharp rise in reflectivity is observed and the coherent phonon oscillations are clearly visible. In contrast, at 166 kV/cm, the initial rise at 0 to 0.4 ps is much slower. Coherent phonon oscillations are completely absent in the signal at this lower pump field strength. These divergent responses suggest the presence of a threshold effect influencing the phonon excitation. To quantify this threshold behavior, we calculated both the average reflectivity change after excitation in the re-

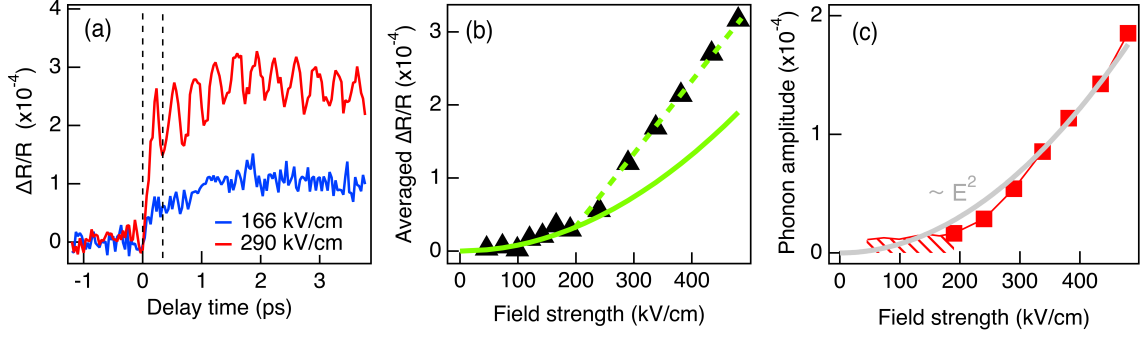


FIG. 3. (a) Time-resolved reflectivity change  $\Delta R/R$  for two representative THz pump field strength of 166 and 290 kV/cm. (b) Average reflectivity change in the time interval of 0 to 0.4 ps labelled by the black dashed lines as a function of THz field strength. (c) Phonon oscillation amplitude as a function of THz field strength. It deviates from the quadratic field dependence (gray curve). Below 200 kV/cm, no phonon oscillations are observed (hatched area).

gion of 0 to 0.4 ps and the amplitude of the coherent phonon oscillation at various THz field strengths. Our full field strength dependent  $\Delta R/R$  data and the details of our analysis methods are provided in Supplementary Material. Figure 3(b) and 3(c) display the average signals and the extracted phonon oscillation amplitude as a function of THz field strength up to 480 kV/cm, respectively. Both plots exhibit a distinct threshold behavior. Below  $\sim 200$  kV/cm, the average  $\Delta R/R$  signal scales with the square of the THz field strength, and the phonon oscillation amplitude remains negligible. As the field strength is beyond 200 kV/cm, the average signal increases at a much faster rate and the phonon oscillation amplitude starts to become significant. This threshold behavior is strongly correlated with the emergence of a fast rising edge and the appearance of the coherent phonon oscillations in our reflectivity data.

Before delving into the details of the excitation mechanism, it is essential to evaluate if current prevailing models can explain our results. THz driving of Raman-active phonons has been observed in various materials and interpreted using either an anharmonic coupling model or a THz sum frequency model [9–13]. Based on our data, we can swiftly exclude the conventional anharmonic coupling model that relies on the presence of zone-center infrared-active optical phonon modes [12, 14]. Bismuth has a rhombohedral A7 lattice structure, with two Bi atoms in each unit cell. The phonon dispersion of the bismuth lattice does not include any zone-center infrared-active optical phonon modes in the THz regime [24, 25]. On the other hand, the THz sum frequency model has been demonstrated in  $\text{CdWO}_4$  and (100)-oriented diamond which are both insulating [11, 13]. It is unclear if this model is still valid in the semimetals like bismuth. Most importantly, the amplitude of the driven phonon from the THz sum frequency mechanism is a quadratic function of the THz field strength [11, 13]. However, the driven phonon amplitude of bismuth, as shown in Figs.

3(c), exhibits a pronounced threshold behavior followed by a quasi-linear dependence on THz field strength, deviating from the quadratic field behavior. These findings suggest that the THz sum frequency process is unlikely to account for our observations.

Elemental bismuth is a semimetal with low carrier density and small band gap [26]. Figure 4(a) presents the schematic band structure of bismuth near the L points, where the band gap  $\mathcal{E}_g$  is approximately 15 meV [27]. Previous studies have demonstrated that the presence of strong electric field can produce additional carriers in the semimetals and semiconductors effectively with narrow band gaps [28, 29]. As illustrated by Figs. 4(a), generally, for electrons in the valence bands to transition into the conduction bands, they must overcome a minimum potential barrier of approximately  $\mathcal{E}_g + \mathcal{E}_F$ , which is significantly larger than the energy of THz photons. Here  $\mathcal{E}_F$  is the Fermi energy. For simplifying this transition problem, we can view the electrons in the valence bands as being bound by a potential barrier  $\mathcal{E}'_g \sim \mathcal{E}_g + \mathcal{E}_F$ . The presence of an intense THz electric field can significantly distort this potential barrier, enabling tunnel ionization where electrons can tunnel through the potential barrier [28, 29]. As a result, a rapid increase of the carrier density is induced, which can be a driving force of Raman-active phonons via DECP mechanism [7].

To see if the rise in carrier density via THz-driven tunnel ionization is sufficiently rapid to initiate the  $A_{1g}$  phonon, we use the following formula, which is valid in the effective mass approximation, to simulate the tunneling rate  $dn/dt$  of valence electrons transitioning to the conduction bands [28].

$$\frac{dn}{dt} = 2\pi \left( \frac{eE_{in}}{2\pi\hbar} \right)^2 \left( \frac{m_1 m_2 m_3}{m_{||}^2 \mathcal{E}'_g} \right)^{\frac{1}{2}} e^{-\frac{\pi}{2e\hbar E_{in}} \sqrt{m_{||}(\mathcal{E}'_g)^3}} \quad (1)$$

Here  $n$  is the injected carrier density.  $E_{in}$  is the THz electric field inside the bismuth film.  $E_{in}$  is related to

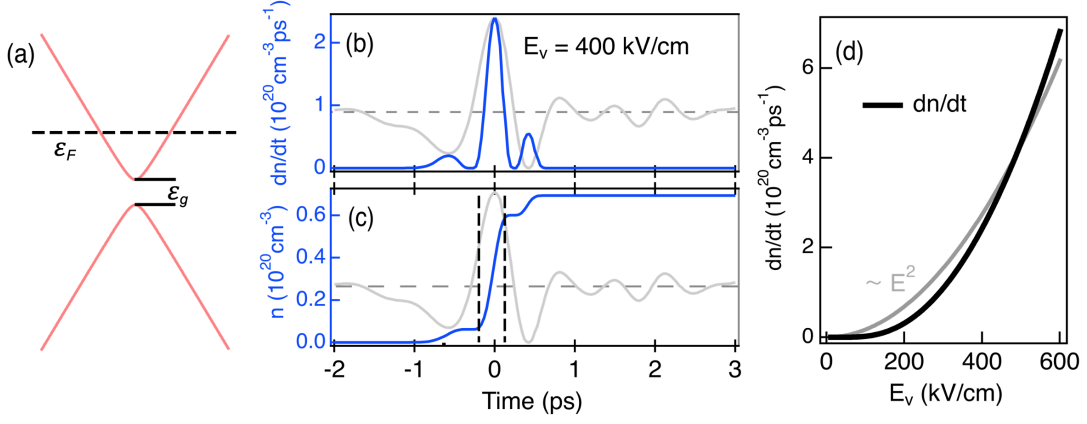


FIG. 4. (a) Schematic for band structure of bismuth near the L points.  $\mathcal{E}_g$  is the band gap and  $\mathcal{E}_F$  is the Fermi energy. (b) The temporal profile of the transient tunneling rate  $dn/dt$  at a field strength of 400 kV/cm. (c) The temporal profile of the transient injected carrier density  $n$  at a field strength of 400 kV/cm. For comparison, the waveform of THz pulse (gray curve) in time domain is also plotted. (d) Simulation of the tunneling rate  $dn/dt$  as a function of THz field strength.  $dn/dt$  deviates from the quadratic field dependence (gray curve)

the THz electric field in vacuum,  $E_v$ , by a factor  $\alpha$ :  $E_{in} = \alpha E_v$ . At room temperature,  $\alpha$  is estimated to be  $\sim 0.25$  (see SM).  $\mathcal{E}'_g$  is the potential barrier and approximately equates  $\mathcal{E}_g + \mathcal{E}_F$ .  $m_1$ ,  $m_2$  and  $m_3$  are determined by  $m_i^{-1} = m_{ic}^{-1} + m_{iv}^{-1}$  ( $i = 1, 2, 3$ ), where 1, 2, and 3 refer to the binary, bisectrix, and trigonal axes, respectively.  $m_{ic}$  and  $m_{iv}$  are the effective masses of the bottom of conduction bands and the top of valance bands, respectively.  $m_{||}$  is determined by  $m_{||}^{-1} = \cos^2\theta/m_1 + \sin^2\theta/m_2$ . Here  $\theta$  is the angle between THz polarization and the principal axis. Before presenting our simulation results, it is worth to emphasize two key points regarding Eq. 4. First, the tunneling rate  $dn/dt$  exhibits an exponential dependence on  $1/E_{in}$ . This leads to a threshold behavior of the tunneling rate with electric field strength. Second, since the tunneling rate near the THz pulse peak scales like  $E_{in}^2$ , there is an effective narrowing of the profile of tunneling rate in the time domain comparing to the duration of the THz pulse. These two key characteristics of Eq. 4 offer the potential to explain our observations.

We take the numerical values of  $m_1$ ,  $m_2$ ,  $m_3$ ,  $\mathcal{E}_g$  and  $\mathcal{E}_F$  from Ref. [27]. For capturing the threshold behavior of the phonon excitation, we rescale these parameters to match the threshold field strength 200 kV/cm determined by our experiments. More details of the simulations are presented in the Supplementary Material. Figure 4(b) shows the simulated temporal profile of  $dn/dt$  at  $E_v = 400$  kV/cm. It is evident that the temporal profile of  $dn/dt$  is much sharper than that of the THz pulse. By integrating  $dn/dt$  over time, we can directly calculate the temporal profile of injected charge density  $n$ . The resulting curve shown in Figs. 4(c) demonstrates a sharp rise in charge density near time zero. This rapid increase, occurring on a timescale of approximately 200 fs, is fast enough to drive the  $A_{1g}$  mode via DECP mechanism in

bismuth [7]. It is well known that the temporal profile of the phonon oscillation driven by DECP mechanisms should follow a cosine function  $\cos\omega_0 t$ , where the initial phase of the driven phonon is zero [7]. Here  $\omega_0$  is the phonon frequency. Our cosine fitting to the phonon oscillation in Figs. 1(b) yields an initial phase  $\sim 0.035\pi$ , which is approximately zero, supporting the DECP-like mechanism enabled by THz-induced tunnel ionization.

We further present the simulated tunneling rate  $dn/dt$  as a function of THz peak field strength in Figs. 4(d). We emphasize two key points. First, the simulation reveals a distinct threshold behavior. This indicates that while THz-driven tunnel ionization leads to a rapid rise, the  $A_{1g}$  mode can only be effectively driven when the injected carrier density reaches a notable level. Below the threshold, the slow rise in  $\Delta R/R$  observed in Figs. 3(a) is likely from the incoherent excitation of intraband transitions, which is not rapid enough to drive the phonon effectively. Second, the field dependence of tunneling rate deviates from the quadratic behavior, causing the driven phonon amplitude, as shown in Figs. 3(c), to also deviate from quadratic behavior. This further strengthens our argument against the THz sum frequency mechanism which enforces a quadratic field dependence [11, 13]. Our simulations in Fig. 4 qualitatively explain the threshold behavior and the synchronous emergence of a sharp rising edge and the coherent  $A_{1g}$  phonon oscillations in  $\Delta R/R$ . It should be noted that our analysis does not include carrier relaxation which need be considered to accurately interpret the extended relaxation of  $\Delta R/R$  on longer time scales. However, it captures the key aspects of THz pulse driven Raman-active phonons in bismuth. Simulations of temporal profiles of  $dn/dt$  and  $n$  for more THz field strengths are provided in Supplementary Material.

The observation of THz-driven Raman-active phonons

via tunnel ionization marks a significant advancement in the research of high-field THz control of materials. THz pulses have demonstrated their efficiency in driving IR-active phonons by coupling to their dipole moments [30, 31], as well as Raman-active phonons through anharmonic coupling to other modes [12, 32]. This capability opens up the exploration of numerous light-induced phase transitions in quantum materials, including light-induced superconductivity, charge density waves, and ferroelectricity [31–34]. Our discovery not only expands the known mechanisms for the excitation of coherent phonons but also highlights the potential for dynamic control over the electronic and structural properties of semimetals and narrow-band semiconductors, especially in material systems where the coherent phonons cannot be driven by conventional mechanisms.

In summary, we studied the THz excitation of the Raman-active  $A_{1g}$  phonon in a bismuth thin film. We showed that this phonon is excited through a DECP type mechanism rather than anharmonic phonon coupling or a THz sum frequency process. We demonstrated that the THz-driven tunnel ionization provides an effective means of sharpening the rising edge of the tunneling carrier density, creating a dispersive driving force triggering the phonon oscillations. This provides an alternative approach to selective control of coherent phonons in solids. Our findings can be easily extended to other semimetals or semiconductors and illustrate the importance of carrier mediated effects like tunnel ionization in experiments using high-field THz pulses.

We would like to thank Liangbo Liang for helpful discussion. Use of the Linac Coherent Light Source, SLAC National Accelerator Laboratory, is supported by the US Department of Energy (DOE), Office of Science, Basic Energy Sciences, under contract no. DE-AC02-76SF00515. The work at SIMES (BC, DAR, JAS, MT and ZXS) is supported by the U.S. Department of Energy (DOE), Office of Science, Basic Energy Sciences, Materials Sciences and Engineering Division under Contract No. DE-AC02-76SF00515; the work at LCLS (PK and M.C.H) is supported by U.S. Department of Energy (DOE), Office of Science, Basic Energy Sciences, under award no. 2018-SLAC-100499. The work at Stony Brook University (M.K.L.) is supported by the NSF Faculty Early Career Development Program under Grant No. DMR-2045425, a QuantEmX travel grant from ICAM, and the Gordon and Betty Moore Foundation through Grant GBMF9616 to M.K.Liu.

---

\* chengbing986@gmail.com

† sobota@stanford.edu

‡ hoffmann@slac.stanford.edu

[1] T. K. Cheng, S. D. Brorson, A. S. Kazeroonian, J. S.

- Moodera, G. Dresselhaus, M. S. Dresselhaus, and E. P. Ippen, *Applied Physics Letters* **57**, 1004 (1990).
- [2] K. Sokolowski-Tinten, C. Blome, J. Blums, A. Cavalleri, C. Dietrich, A. Tarasevitch, I. Uschmann, E. Forster, M. Kammler, M. Horn-von Hoegen, et al., *Nature* **422**, 287 (2003).
- [3] D. M. Fritz, D. A. Reis, and et al., *Science* **315**, 633 (2007).
- [4] A. de la Torre, D. M. Kennes, M. Claassen, S. Gerber, J. W. McIver, and M. A. Sentef, *Rev. Mod. Phys.* **93**, 041002 (2021).
- [5] S. De Silvestri, J. Fujimoto, E. Ippen, E. B. Gamble, L. R. Williams, and K. A. Nelson, *Chemical Physics Letters* **116**, 146 (1985).
- [6] G. A. Garrett, T. F. Albrecht, J. F. Whitaker, and R. Merlin, *Phys. Rev. Lett.* **77**, 3661 (1996).
- [7] H. J. Zeiger, J. Vidal, T. K. Cheng, E. P. Ippen, G. Dresselhaus, and M. S. Dresselhaus, *Phys. Rev. B* **45**, 768 (1992).
- [8] J. J. Li, J. Chen, D. A. Reis, S. Fahy, and R. Merlin, *Phys. Rev. Lett.* **110**, 047401 (2013).
- [9] L. Braun, *Electron and Phonon Dynamics in Topological Insulators at THz Frequencies* (Freie Universität, Berlin, Germany, 2016).
- [10] P. Bowlan, J. Bowlan, S. A. Trugman, R. V. Aguilar, J. Qi, X. Liu, J. Furdyna, M. Dobrowolska, A. J. Taylor, D. A. Yarotski, et al., *Optica* **4**, 383 (2017).
- [11] S. Maehrlein, A. Paarmann, M. Wolf, and T. Kampfrath, *Phys. Rev. Lett.* **119**, 127402 (2017).
- [12] A. A. Melnikov, K. N. Boldyrev, Y. G. Selivanov, V. P. Martovitskii, S. V. Chekalin, and E. A. Ryabov, *Phys. Rev. B* **97**, 214304 (2018).
- [13] C. L. Johnson, B. E. Knighton, and J. A. Johnson, *Phys. Rev. Lett.* **122**, 073901 (2019).
- [14] A. A. Melnikov, Y. G. Selivanov, and S. V. Chekalin, *Phys. Rev. B* **102**, 224301 (2020).
- [15] F. Giorgianni, M. Udina, T. Cea, E. Paris, M. Caputo, M. Radovic, L. Boie, J. Sakai, C. W. Schneider, and S. L. Johnson, *Communications Physics* **5**, 1 (2022).
- [16] J. Hebling, G. Almási, I. Z. Kozma, and J. Kuhl, *Opt. Express* **10**, 1161 (2002).
- [17] M. Forst, C. Manzoni, S. Kaiser, Y. Tomioka, Y. Tokura, R. Merlin, and A. Cavalleri, *Nat. Phys.* **7**, 854 (2011).
- [18] M. Hase, K. Mizoguchi, H. Harima, S. Nakashima, M. Tani, K. Sakai, and M. Hangyo, *Applied Physics Letters* **69**, 2474 (1996).
- [19] K. Ishioka, M. Kitajima, and O. V. Misochko, *Journal of Applied Physics* **100**, 093501 (2006).
- [20] A. Melnikov, O. Misochko, and S. Chekalin, *Physics Letters A* **375**, 2017 (2011).
- [21] Y. M. Sheu, Y. J. Chien, C. Uher, S. Fahy, and D. A. Reis, *Phys. Rev. B* **87**, 075429 (2013).
- [22] A. Koç, I. Gonzalez-Vallejo, M. Runge, A. Ghalgaoui, K. Reimann, L. Kremeyer, F. Thiemann, M. H.-v. Hoegen, K. Sokolowski-Tinten, M. Woerner, et al., *Phys. Rev. B* **107**, L180303 (2023).
- [23] M. Runge, A. Ghalgaoui, I. Gonzalez-Vallejo, F. Thiemann, M. Horn-von Hoegen, K. Reimann, M. Woerner, and T. Elsaesser, *Phys. Rev. B* **107**, 245140 (2023).
- [24] E. D. Murray, S. Fahy, D. Prendergast, T. Ogitsu, D. M. Fritz, and D. A. Reis, *Phys. Rev. B* **75**, 184301 (2007).
- [25] Y. Zhao, S. Clément, J. Haines, and R. Vienneis, *The Journal of Physical Chemistry C* **124**, 26659 (2020).
- [26] N. P. Armitage, R. Tediosi, F. Lévy, E. Giannini,

- L. Forro, and D. van der Marel, Phys. Rev. Lett. **104**, 237401 (2010).
- [27] R. T. Isaacson and G. A. Williams, Phys. Rev. **185**, 682 (1969).
- [28] L. V. Keldysh, J. Exp. Theor. Phys. **33**, 994 (1958).
- [29] L. V. Keldysh, J. Exp. Theor. Phys. **20**, 1307 (1964).
- [30] B. Cheng, T. Schumann, Y. Wang, X. Zhang, D. Barbalas, S. Stemmer, and N. P. Armitage, Nano Letters **20**, 5991 (2020).
- [31] B. Cheng, P. L. Kramer, Z.-X. Shen, and M. C. Hoffmann, Phys. Rev. Lett. **130**, 126902 (2023).
- [32] M. Mitrano, A. Cantaluppi, D. Nicoletti, S. Kaiser, A. Perucchi, S. Lupi, P. Di Pietro, D. Pontiroli, M. Riccò, S. R. Clark, et al., Nature **530**, 461 (2016).
- [33] X. Li, T. Qiu, J. Zhang, E. Baldini, J. Lu, A. M. Rappe, and K. A. Nelson, Science **364**, 1079 (2019).
- [34] T. F. Nova, A. S. Disa, M. Fechner, and A. Cavalleri, Science **364**, 1075 (2019).
- [35] B. Cheng, N. Kanda, T. N. Ikeda, T. Matsuda, P. Xia, T. Schumann, S. Stemmer, J. Itatani, N. P. Armitage, and R. Matsunaga, Phys. Rev. Lett. **124**, 117402 (2020).
- [36] Y. Hirail, N. Yoshikawa, M. Kawaguchi, M. Hayashi, S. Okumura, T. Oka, and R. Shimano, arXiv. **2301**, 06072 (2023).

### Supplementary Note 1: THz-pump optical-probe setup

The schematic of our THz pump optical probe setup is depicted in Fig. S1. The single-cycle THz pulses were generated by optical rectification of 130 fs 800 nm laser pulses with 4 mJ energy using the tilted pulse front method in LiNbO<sub>3</sub>. The THz pulses with energies up to 3  $\mu$ J were focused onto the sample yielding a spot size of about  $1.2 \times 1.2$  mm<sup>2</sup> and a fluence of  $\approx 0.2$  mJ/cm<sup>2</sup>. The THz field strength at the focus was measured by electro optical (EO) sampling in a 100  $\mu$ m thick 110-cut GaP crystal. The maximum field strength was  $\sim 500$  kV/cm. The waveform of THz pulse in time domain is displayed in main text Fig. 2. A pair of wire grid polarizers, controlled by a computerized rotation stage, was used to continuously attenuate the THz field. The linearity of this attenuation was verified by EO sampling. Weak probe pulses at 800 nm wavelength were directed onto the sample collinearly with the THz beam, and then reflected onto a photo diode by slightly tilting the sample. A part of the probe beam was split off before the sample and directed onto a second, identical, photo diode for balanced detection, minimizing laser noise. All measurements in this work were performed at room temperature.

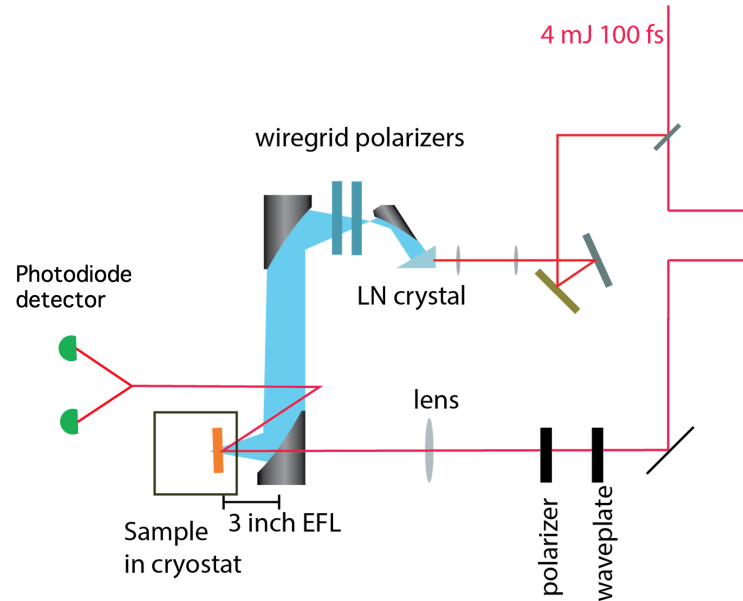


FIG. S1. (Color online) The schematic of our THz pump optical probe setup.

### Supporting Note 2: Full reflectivity data as a function of terahertz field strength

In Fig. S2, we show the reflectivity change  $\Delta R/R$  of bismuth thin film as a function of delay time between THz pump and 800 nm probe pulses at various THz field strengths. One can see that below 200 kV/cm, the initial rise of  $\Delta R/R$  at 0 to 0.4 ps is much slower. In the meanwhile, the coherent phonon oscillations are completely absent in the signals. In contrast, above 200 kV/cm, a sharp rise in reflectivity gradually develops and the coherent phonon oscillations are clearly visible. This full dataset is completely consistent with the excitation threshold behavior of the coherent phonon discussed in the main text.

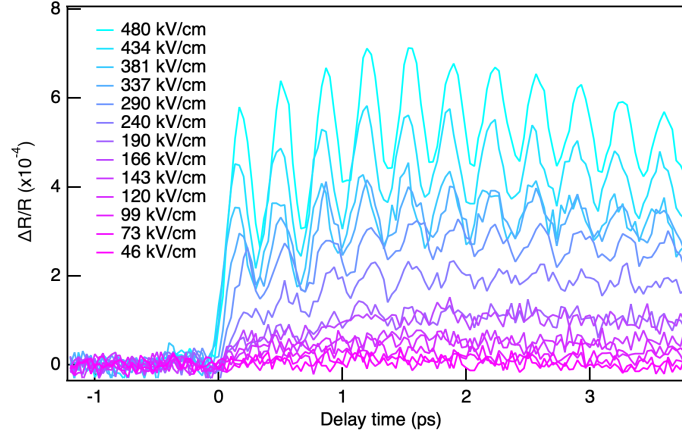


FIG. S2. (Color online) The reflectivity change  $\Delta R/R$  of bismuth thin film as a function of delay time at various THz field strengths.



### Supporting Note 3: Substraction of electronic background

To extract the THz field strength dependent phonon amplitude, one needs to subtract the electronic background of the reflectivity change  $\Delta R/R$  first. We used a polynomial function convolving with the step function to capture the electronic background. The equation is shown below.

$$\Delta R/R = a_0 + (k_0 + k_1 t + k_2 t^2 + k_3 t^3 + k_4 t^4)(1 + \text{erf}(2\sqrt{\ln 2}(t - t_0)/w))/2 \quad (1)$$

Here  $a_0$  is the constant offset.  $k_0, k_1, k_2, k_3$ , and  $k_4$  are the coefficients of the polynomial.  $t_0$  is the time zero.  $\text{erf}$  is the error function to simulate the rise of  $\Delta R/R$ .  $w$  is the rise width. Note that in this work, we are only interested in THz pump field strength dependence of the phonon amplitude. The way to simulate electronic background will not modify the pump field strength dependence of phonon oscillations. The polynomial fitting is the easiest way to capture the electronic background. We will not discuss the physics meaning of these fitting. Our aim is only to isolate the phonon oscillations. We present all data fitting in Fig. S3. One can see the polynomial fitting can reasonably capture the electronic background. All residual phonon oscillation data are present in Fig. S4.

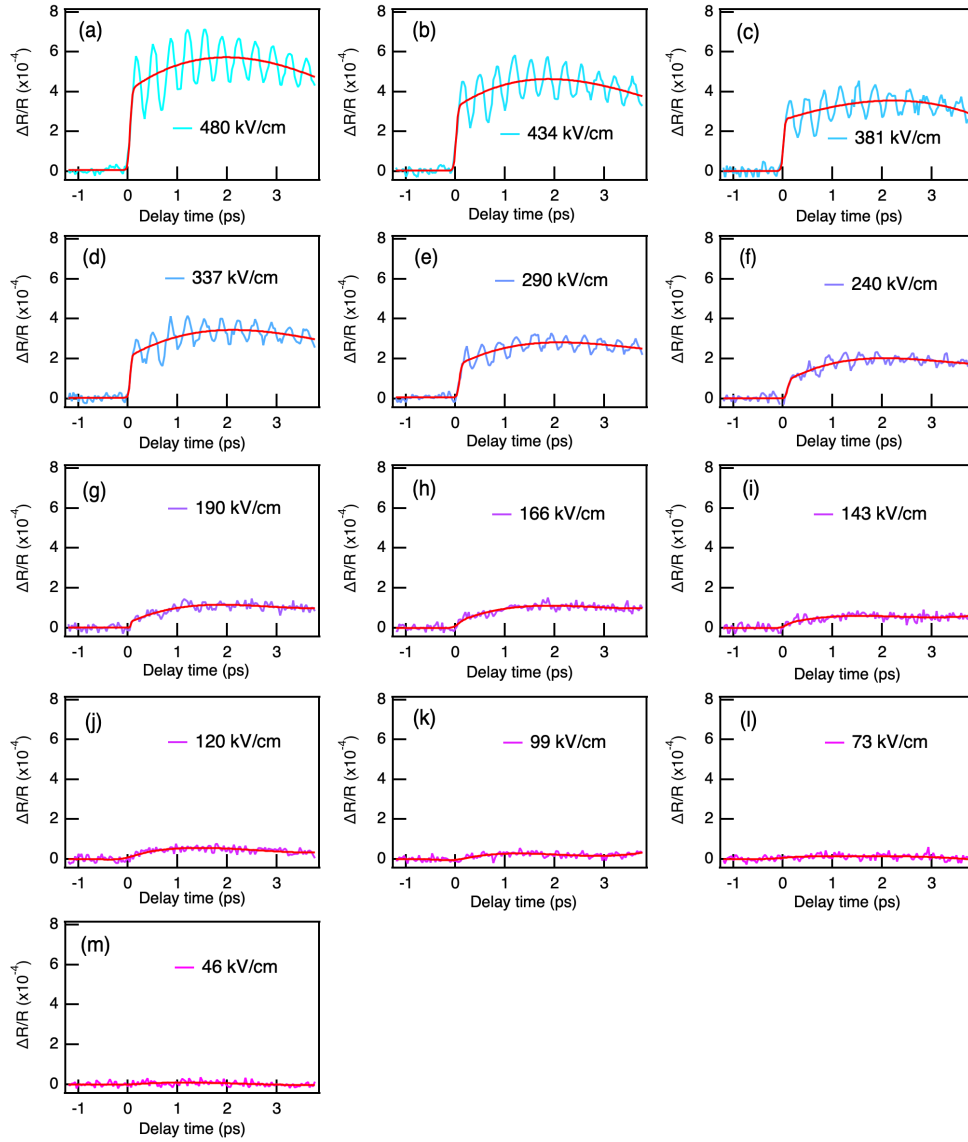


FIG. S3. (Color online) The fitting of the electronic background of  $\Delta R/R$  at various THz field strengths.



### Supporting Note 4: Fits of the phonon amplitude

To extract the THz field strength dependent phonon amplitude, we used a cosine function convolving with an exponential decaying function to fit the phonon oscillations. The equation is shown below.

$$\Delta R/R = A \cos(2\pi f(t - t_0) + \phi_0) * \exp(-(t - t_0)/\tau) \quad (2)$$

Here  $A$  is the phonon amplitude.  $f$  is the phonon frequency.  $t_0$  is the time zero.  $\tau$  is the decay constant.  $\phi_0$  is the initial phase of the phonon oscillations. We present all fittings in Fig. S4. The fittings reasonably capture all the phonon oscillations data above 200 kV/cm. Below 200 kV/cm, the phonon oscillations are not visible in the signals. We present the phonon oscillation amplitude as a function of THz field strength in the Fig. 3(c) of main text. Note that below 200 kV/cm, we do not observe phonon oscillations. Any fittings to these data become meaningless. We calculated the standard deviation of each curve in Fig. S4(g) and then plotted them as the hatched region in Fig. 3(c) of main text. This hatched region represents the upper limit on the phonon amplitude below 200 kV/cm.

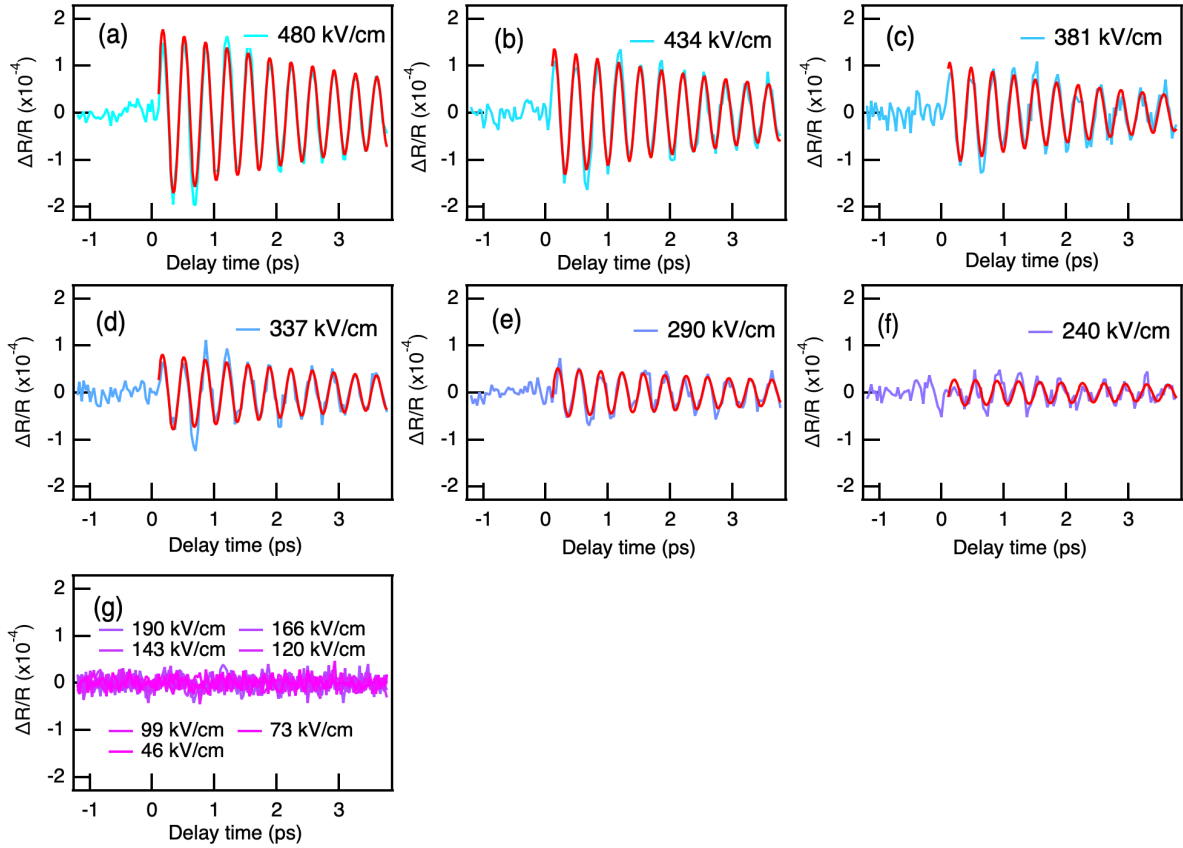


FIG. S4. (Color online) The fitting of the phonon oscillations at various THz field strengths.

### Supporting Note 5: Estimation of THz field strength inside the bismuth film

To simulate the tunneling rate  $dn/dt$ , we need to know the THz field strength  $E_{in}$  inside the bismuth film.  $E_{in}$  is related to the THz electric field in vacuum,  $E_v$ , by a factor  $\alpha$ :  $E_{in} = \alpha E_v$ . Here the coefficient  $\alpha$  is determined by the following formula [35].

$$\alpha = \frac{1}{1 - \frac{n_b - 1}{n_b + 1} \frac{n_b - n_s}{n_b + n_s} e^{2i \frac{\omega d n_b}{c}}} \frac{2}{n_b + 2} \left( 1 + \frac{n_b - n_s}{n_b + n_s} e^{2i \frac{\omega d n_b}{c}} \right) \quad (3)$$

Here  $n_b$  is the complex refractive index of the bismuth thin film.  $n_s$  (3.3) is the refractive index of the sapphire substrate in THz regime.  $d$  (50 nm) is the thickness of the bismuth film. To determine  $\alpha$  at room temperature, we need to know the refractive index of the bismuth thin film  $n_b$  at the room temperature. We used the terahertz conductivity data of bismuth thin film in Ref. [36] to estimate  $n_b$ . Note that Ref. [36] only provides terahertz conductivity data of bismuth film at 25 K. Bismuth is a semimetal so that its room temperature conductivity is usually larger than the conductivity at 25 K. For simplicity, we rescale a factor of 2 to the data at 25 K and use this rescaled data as room temperature terahertz conductivity. Then  $n_b$  at room temperature is determined by  $n_b = \sqrt{1 + \frac{i\sigma(\omega)}{\epsilon_0\omega}}$ . Here  $\epsilon_0$  is the permittivity of free space.  $\sigma(\omega)$  is the optical conductivity.  $\omega$  is the angular frequency. Fig. S4(b) presents the simulation of  $\alpha$  at room temperature using  $\sigma$  in Fig. S4(a).  $\alpha$  shows very weak frequency dependence below 2 THz. We take  $\alpha \sim 0.25$  to simulate the tunneling rate  $dn/dt$  at room temperature.

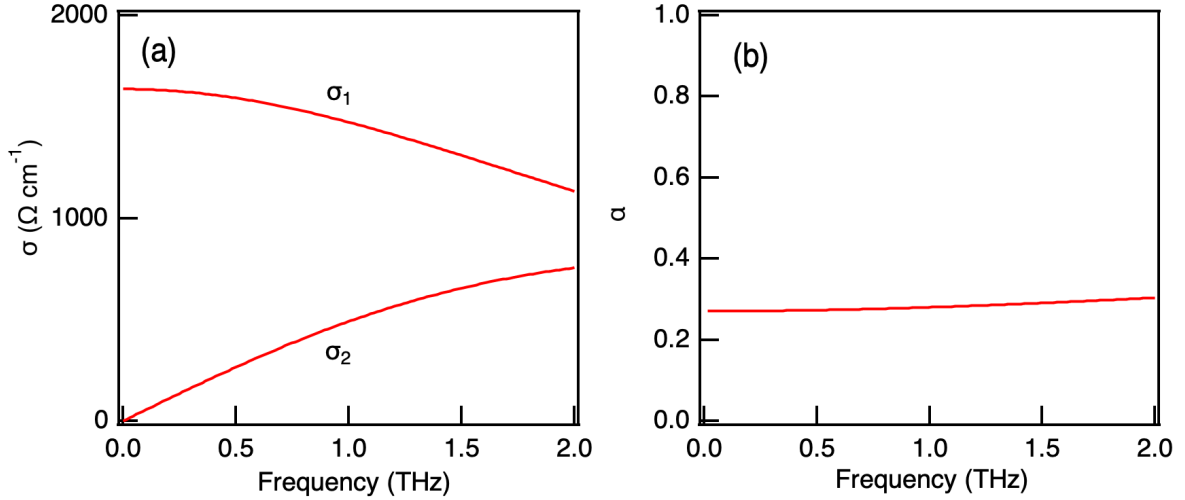


FIG. S5. (Color online) (a) Optical conductivity of bismuth thin film at room temperature estimated from the data presented in Ref. [36]. (b) The simulation result of  $\alpha$ .

### Supporting Note 6: Simulation of THz field driving tunnel ionization in bismuth thin film

In the main text, we used below formula to simulate the tunneling rate  $dn/dt$  induced by THz pulses in the bismuth film [28].

$$\frac{dn}{dt} = 2\pi \left( \frac{eE_{in}}{2\pi\hbar} \right)^2 \left( \frac{m_1 m_2 m_3}{m_{||}^2 \mathcal{E}'_g} \right)^{\frac{1}{2}} e^{-\frac{\pi}{2e\hbar E_{in}} \sqrt{m_{||}(\mathcal{E}'_g)^3}} \quad (4)$$

Here  $n$  is the injected carrier density.  $E_{in}$  is the THz electric field inside the bismuth film.  $E_{in}$  is related to the THz electric field in vacuum,  $E_v$ , by a factor  $\alpha$ :  $E_{in} = \alpha E_v$ . At room temperature,  $\alpha$  is estimated to be  $\sim 0.25$ .  $\mathcal{E}'_g$  is the energy barrier and approximately equates  $\mathcal{E}_g + \mathcal{E}_F$ .  $\mathcal{E}_F$  is the Fermi energy.  $m_1$ ,  $m_2$  and  $m_3$  are determined by  $m_i^{-1} = m_{ic}^{-1} + m_{iv}^{-1}$  ( $i = 1, 2, 3$ ), where 1, 2, and 3 refer to the binary, bisectrix, and trigonal axes, respectively.  $m_{ic}$  and  $m_{iv}$  are the effective masses of the bottom of conduction bands and the top of valance bands, respectively.  $m_{||}$  is determined by  $m_{||}^{-1} = \cos^2\theta/m_1 + \sin^2\theta/m_2$ . Here  $\theta$  is the angle between THz polarization and the principal axis.

We take the numerical values of  $m_1$ ,  $m_2$ ,  $m_3$ ,  $\mathcal{E}_g$  and  $\mathcal{E}_F$  from the ref 4, where  $m_1^{-1} = (1.4 \times 10^{-3}m_0)^{-1} + (6.5 \times 10^{-3}m_0)^{-1}$ ,  $m_2^{-1} = (0.29m_0)^{-1} + (1.36m_0)^{-1}$ ,  $m_3^{-1} = (7 \times 10^{-3}m_0)^{-1} + (2.97 \times 10^{-2}m_0)^{-1}$ ,  $\mathcal{E}_g = 15$  meV, and  $\mathcal{E}_F = 27$  meV. Here  $m_0$  is the mass of electron [27]. It is important to note that the ionization rate is nearly independent of the crystallographic direction when taking into account all 3 L-points. For simplicity, we take  $\theta = 0$  to determine  $m_{||}$ . After inputting these parameters into Eq. 4, we obtain the tunneling rate  $dn/dt$  as a function of THz peak electric field as shown in Fig. S6(a) (blue curve). It clearly shows a threshold like behavior with increasing field. Unfortunately, the threshold field strength is about 80 kV/cm, two times smaller than the threshold field strength  $\sim 200$  kV/cm determined by our experiments. We noticed that the parameters we used are from the measurements of bismuth single crystals. However, we measured bismuth thin films. It is reasonable to expect that there exists some differences of these parameters in bismuth single crystals and thin films. To capture the threshold behavior of the phonon excitation, we rescale the parameters in the exponential part of Eq. 4 to match the threshold field strength 200 kV/cm revealed in the Fig. 3 of main text. The black curve in Fig. S6(a) represents the result after doing rescaling. Now we can see the threshold behavior at field strength  $\sim 200$  kV/cm is reasonably reproduced. We present temporal profiles of tunneling rate  $dn/dt$  at various THz peak field strengths in Fig. S6(b). By integrating  $dn/dt$  over time, we can directly calculate the temporal profile of injected charge density  $n$ . The resulting curves are shown in Fig. S6(c). One can see that both quantities are negligible below 150 kV/cm, indicting the threshold like behavior. At the same time, the temporal profile of injected charge density  $n$  develops a rapid rise edge. We used a step function  $(1 + \text{erf}(2\sqrt{\ln 2}(t - t_0)/w))/2$  to fit the rise time. Here  $t_0$  is the time zero.  $\text{erf}$  is the error function.  $w$  is the rise width. The fitting result is presented in Fig. S6(d). The rise time is found to be  $\sim 200$  fs, which is fast enough to drive the  $A_{1g}$  mode in bismuth.

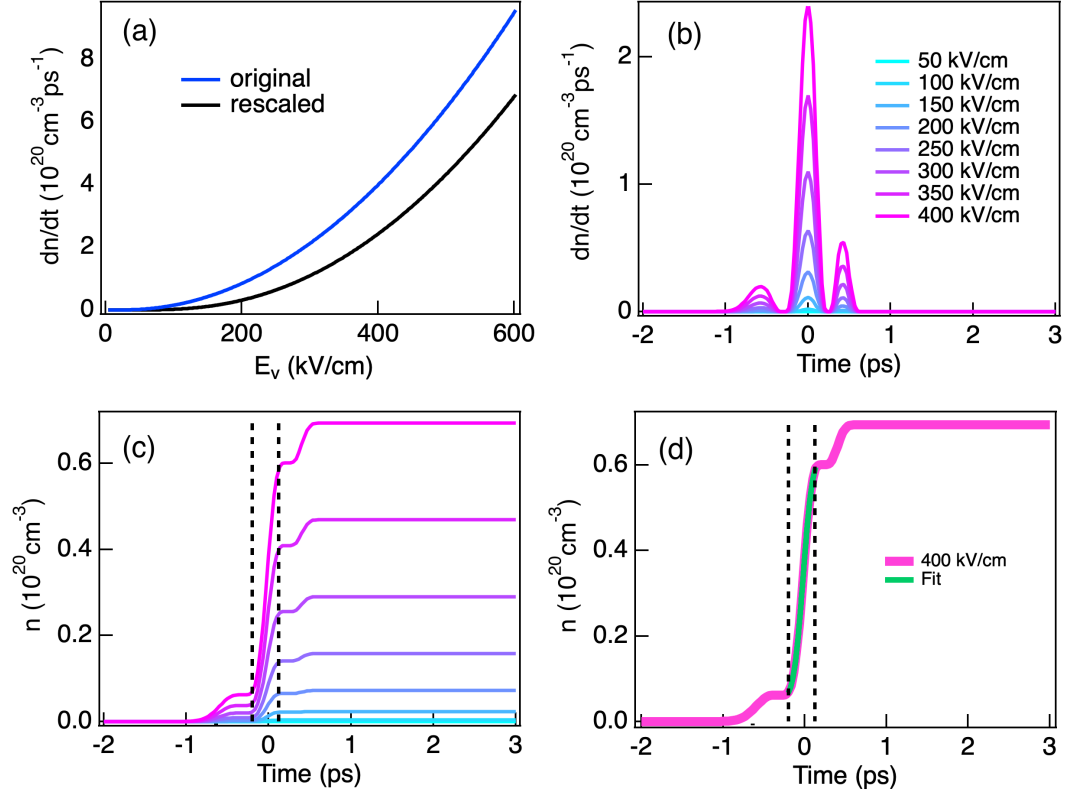


FIG. S6. (Color online) (a) Simulation of the tunneling rate  $dn/dt$  as a function of THz electric field strength. (b) The temporal profile of the transient tunneling rate  $dn/dt$  at various THz field strengths. (c) The temporal profile of the transient injected carrier density  $n$  at various THz field strengths. (d) The fit of the rise edge of the transient injected carrier density  $n$  at a field strength of 400 kV/cm.